Earth Planet. Sci. Lett. 647 (2024) 119058

Contents lists available at ScienceDirect

Earth and Planetary Science Letters

journal homepage: www.elsevier.com/locate/epsl

Correlating 300 million years of catastrophes

Alexei V. Ivanov

Institute of the Earth's Crust, Siberian Branch of the Russian Academy of Sciences, 128 Lermontov Street, Irkutsk 664033, Russia

ARTICLE INFO

Editor: Dr A Webb

Keywords:
Large igneous province volcanism
Bolide impact
CO_2 in the atmosphere
Environmental catastrophes
Monte Carlo test

ABSTRACT

It is frequently proposed that large bolide impacts and voluminous volcanic eruptions may be responsible for environmental catastrophes. In the conventional approach, the potential causes and consequences are matched using an age-versus-age plot, with preferential ages selected for comparison. This approach inevitably results in a one-to-one correlation, which may be misleading. To address this issue, a novel statistical metric, named conformity, has been proposed which accounts for the possibility of age coincidence resulting from random processes (i.e. bad luck coincidence). The available and updated geochronological datasets of bolide impacts, large igneous provinces, CO_2-concentration peaks in the atmosphere, mass extinctions, ocean anoxic events, and climatic optima and thermal highs were subjected to a comparison in terms of their concordance. The most significant discovery is the correlation between the ages of mass extinctions and those of giant bolide impacts (crater diameter >40 km), as well as volcanism of continental large igneous provinces and CO_2-concentration peaks in the atmosphere. The severity of mass extinctions appears to be dependent upon the number of simultaneously occurring causes. The most pronounced Late Maastrichtian (~66 Ma) and Changhsingian (~252 Ma) mass extinctions were likely caused by a combination of factors, including the simultaneous occurrence of volcanism of continental large igneous provinces, giant bolide impact and CO_2-concentration rise in the atmosphere. Conversely, the ages of large igneous provinces, bolide impacts and CO_2-concentration peaks are not correlated, indicating that these three causes were not interdependent.

1. Introduction

Vogt (1972) was the first to propose a hypothesis of synchrony between voluminous volcanic events and faunal mass extinctions, focusing on the age coincidence of the Deccan Traps and the Cretaceous-Paleogene faunal extinction. Later, when a sufficient amount of geochronological data had accumulated, Courtillot and Renne (2003) reported that the ages of several environmental catastrophes and some volcanic events were closely correlated (Fig. 1a), and suggested that large volcanic eruptions could trigger environmental catastrophes. Since then, the age correlation between volcanism and environmental catastrophes has gained increasing appeal (Green et al., 2022). A competing hypothesis began with the discovery of an Ir-rich bolide-impact related layer between Cretaceous and Paleogene strata by Alvarez et al. (1980). It suggests that at least some major environmental catastrophes were caused by bolide impacts. Phipps Morgan et al. (2004) noted a possible temporal coincidence of volcanism, impact signatures and mass extinctions. However, they suggested that terrestrial processes could produce some signatures that are interpreted as traces of bolide impacts, while the remaining unquestioned impact-volcanism-extinction coincidences could be due to chance (termed "bad luck coincidences"). Glikson (2005) criticised the work of Phipps Morgan et al. (2004) and showed that there are more age matches between environmental catastrophes, volcanic and bolide impact events (Fig. 1b,c). Using the conventional approach introduced by Courtillot and Renne (2003), one might suggest that environmental catastrophes were controlled by clusters of terrestrial anomalous volcanism and bolide impacts (Glikson, 2005). However, comparing the dates of different events on age-versus-age plots can be erroneous because only the ages that match are plotted and others that do not are omitted. It is the primary purpose of this paper to warn that such matching of pre-selected ages of potential cause and effect is misleading. The second purpose is to develop a procedure for such an age matching test. Finally, this procedure is applied to the analysis of existing and newly collected datasets of various environmental catastrophes, atmospheric CO_2 concentration peaks, bolide impact events and anomalous volcanic events of the last 300 million years.

E-mail address: aivanov@crust.irk.ru.

https://doi.org/10.1016/j.epsl.2024.119058
Received 24 June 2023; Received in revised form 16 September 2024; Accepted 5 October 2024
Available online 8 October 2024

2. Problems of conventional approaches of age matching

The conventional approach of matching the ages of volcanic events to the ages of mass extinctions, as illustrated in Fig. 1, is problematic due to the vast discrepancy in the number of events. It is challenging to justify the rationale behind the selection of a specific volcanic event and the exclusion of another. The preselection of those ages of potential causes (in this example, a volcanic event) that closely match the expected consequence (in this example, a mass extinction) inevitably results in the creation of datasets that are correlated with each other. To demonstrate this, a series of values were randomly generated to resemble geochronological data (Supplement 1: Table S1). It can be observed that some matching values can be identified among the samples with randomly generated values. To illustrate, when two samples comprising 30 random pairs of values, with a similar 1–3 % uncertainty, are considered, 10 pairs are found to be matched (Fig. 2a). A search for matching pairs between 30 randomly generated values with 1–3 % uncertainty and 15 randomly generated values with 0.1–0.3 % uncertainty yielded four matches (Fig. 2b). Even when a sample comprising just five random values with 0.1–0.3 % uncertainty is compared to a sample comprising 30 random values and 10 times larger uncertainty, three matches are still identified (Fig. 2c). Consequently, the use of only matched ages in an age-versus-age plot results in the generation of a strong correlation with a one-to-one slope. Furthermore, this phenomenon is amplified with an increase in sample size (n), due to the reduction in standard deviation with the square root of n (Cramer, 1946). This indicates that the conventional approach of visualising data, whereby a hypothetical cause is plotted in a diagram or listed in a table versus a considered consequence, is inadequate. In order to ascertain the likelihood of a bad-luck coincidence, the data must be evaluated statistically.

Given that the conventional age-versus-age plot is not applicable in this instance, it is necessary to employ an alternative metric. A comparable task of age comparison for their degree of sameness, dissimilarity, or correspondence is frequently encountered in detrital zircon chronology studies (Gehrels, 2000; Powerman et al., 2021; Satkoski et al., 2013; Saylor and Sundell, 2016; Sharman et al., 2018; Sundell and Saylor, 2017,2021; Tye et al., 2019; Vermeesch, 2013,2018a). A review of the various statistical approaches, their respective strengths and limitations, can be found in Saylor and Sundell (2016). In their study, the reliability of commonly used coefficients, including the Kolmogorov-Smirnov (KS) test, Kuiper test, similarity, likeness, and cross-correlation, was evaluated using three criteria. Saylor and Sundell (2016) proposed that when applied to a probability distribution function (PDF), the cross-correlation coefficient fulfils all three criteria. If two samples are identical, the cross-correlation coefficient is unity; conversely, if the samples share no age peaks, the coefficient is zero.

Two issues pertaining to the utilisation of PDFs cross-correlation metrics in this investigation warrant consideration. Firstly, the method demonstrates consistent discrimination between same versus different age populations (coefficient > 0.8), with the analysis commencing at 300 ages. Nevertheless, even for the most similar populations, the coefficient may be <0.5 for a number of ages below 100. To illustrate, the number of ages compared by Courtillot and Renne (2003) and Glikson (2005) is approximately 20 (see Fig. 1a, b, c). Secondly, the coefficient is sensitive not only to the degree of overlap in the age ranges, but also to the shape of the age peaks. While this may be advantageous in detrital chronology when a large number of ages are compared, in this study it will artificially degrade the degree of similarity between the ages of potential causes, which may be uncertain by millions of years, and the precisely dated expected consequence, which may be uncertain by tens or hundreds of thousands of years. To demonstrate this, a PDF cross-correlation was applied to randomly generated subsets (Supplement 1: Table S1) using the DZstats2.30 software (Saylor and Sundell, 2016). The cross-correlation of the PDFs for samples 1 and 2 of random values yields a value of zero, which accurately reflects the dissimilarity between the two random populations. For the same random samples 1 and 2, the likeness is 0.314, the similarity is 0.496, the K-S D-statistic is 0.300, the K-S ρ-value is 0.109, the Kuiper test V-statistic is 0.333 and the Kuiper test ρ-value is 0.313. The application of the PDF cross-correlation to a set of 10 matched values, as illustrated in Fig. 2a, yields a value of 0.548, indicating a high degree of similarity between the preselected, matched values. For the same matched subsample values, the results are as follows: the likeness is 0.645, the similarity is 0.870, the K-S D-statistics is 0.100, the K-S ρ-value is 1, the Kuiper test V-statistics is 0.200 and the Kuiper test ρ-value is 1. It should be noted that the K-S and Kuiper tests indicate that the two subsamples with the preselected matched values belong to the same population. Nevertheless, if the uncertainty is reduced tenfold for one of the subsamples of matched values, the PDFs Cross-correlation drops to 0.142, while the KS and Kuiper ρ-values remain at 1. A more comprehensive examination of the issues associated with the use of the likeness, the cross-correlation, and the ρ-values can be found in Vermeesch (2013, 2018a). For an overview of the general issues associated with the use of

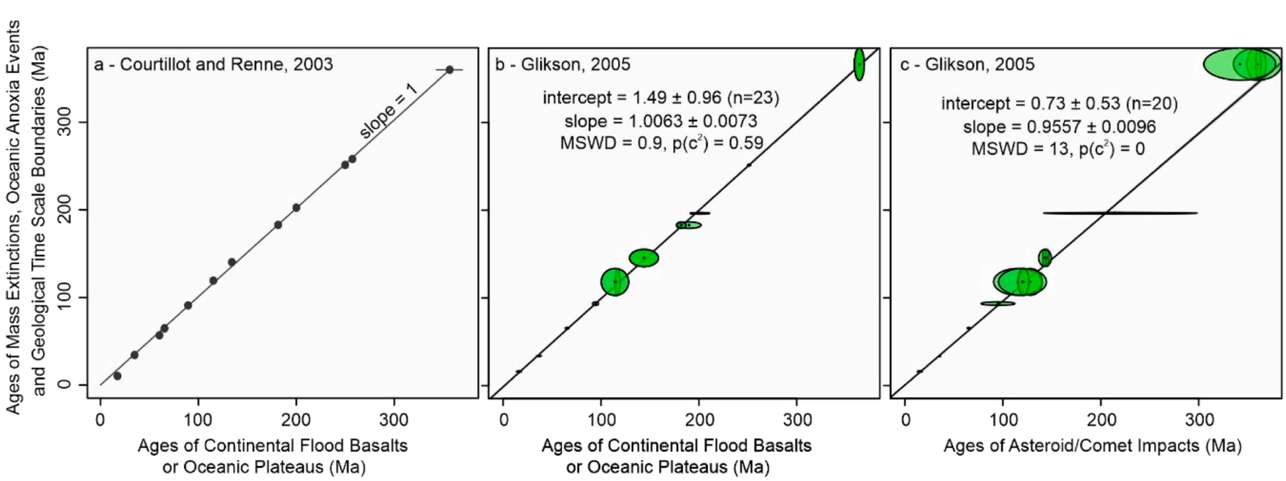

Fig. 1. Age-versus-age plots (a) comparing those of mass extinctions, oceanic anoxic events and geological time scale boundaries with ages of continental flood basalts and/or oceanic plateaus (redrawn with simplifications from Courtillot and Renne, 2003), (b) and (c) the same type of plots using data from Glikson (2005). Note that Glikson (2005) did not use exactly the same environmental events and used slightly different ages for volcanic events compared to the work of Courtillot and Renne (2003). Plots in b and c were constructed and regressions calculated using IsoplotR (Vermeesch, 2018a). Note: Courtillot and Renne (2003) did not provide uncertainties for most of the ages, which prevents direct application of IsoplotR.

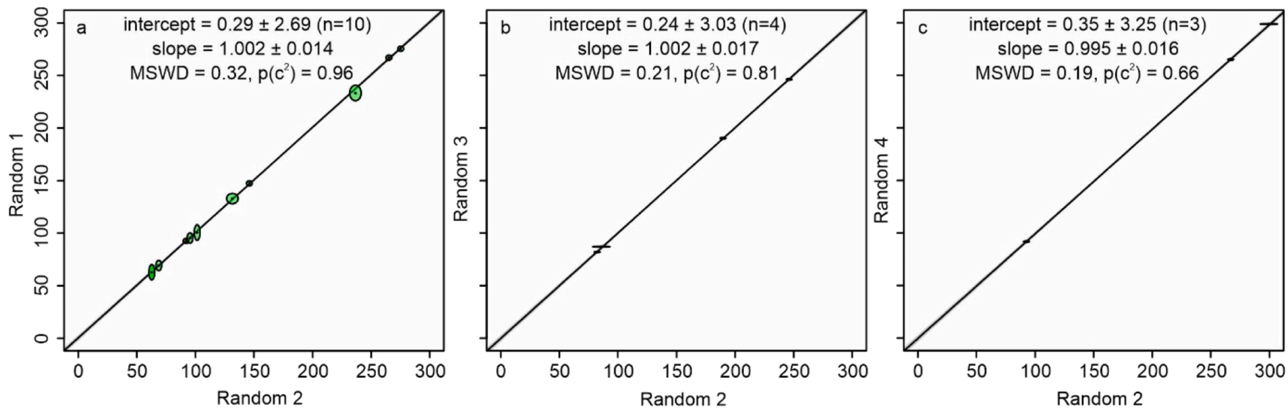

Fig. 2. A value-versus-value plot for matching values of randomly generated samples (Table S1). This approach is analogous to the conventional method of identifying the optimal age matches in a geological record. The plots have been constructed and the regressions calculated using IsoplotR (Vermeesch, 2018b).

ρ-values, please refer to the paper by Wasserstein et al. (2019).

3. Monte Carlo implementation to age matching

The present study assesses the reliability of conventional statistical metrics through the utilisation of Monte Carlo simulations. A novel metric, designated as conformity, is proposed. It can be applied to any metrics, including KS, Kuiper, similarity, likeness, or cross-correlation. However, for this study, where databases vary in structure, with some samples containing a greater number of values than others, and where uncertainty varies significantly between samples and between values within a sample, the similarity metric was found to be the most useful.

The calculation of conformity (C) is as follows: Firstly, a similarity coefficient is calculated for the two sets of real age data that are to be compared. Subsequently, datasets comprising randomly generated values within the same range and with the same uncertainties as those observed in the real data are generated using the Monte Carlo method. To illustrate, consider a real dataset of values within a specified range, namely 0 to 300. These values are 15.83 ± 1.17, 40.2 ± 0.3, 51.1 ± 2.06, and 56.125 ± 0.141. A set of values is generated using Monte Carlo, with limits between 0 and 300. The randomly generated values are then augmented randomly with the selected uncertainty values being 1.17, 0.3, 2.06, and 0.141. Thirdly, the mean (x) and standard deviation (σ) are calculated for the dataset of random values. Subsequently, the C value is calculated between the real similarity coefficient and the Monte Carlo-generated similarity coefficient in terms of standard deviation. This is expressed as follows:

$$C = \frac{x(S) - \langle x \rangle (SS)}{\sigma(SS)}, \quad (1)$$

where *x(S)* is the similarity coefficient calculated for the real dataset, $<x>(SS)$ – the mean value of the simulated similarity coefficient calculated for the Monte Carlo-generated dataset, $\sigma(SS)$ is the standard deviation of the simulated Monte Carlo-generated dataset. It should be noted that the formula (1) is identical to that used for z-score calculation in conformity assessment (ISO/IEC 17043:2023), which is reflected in

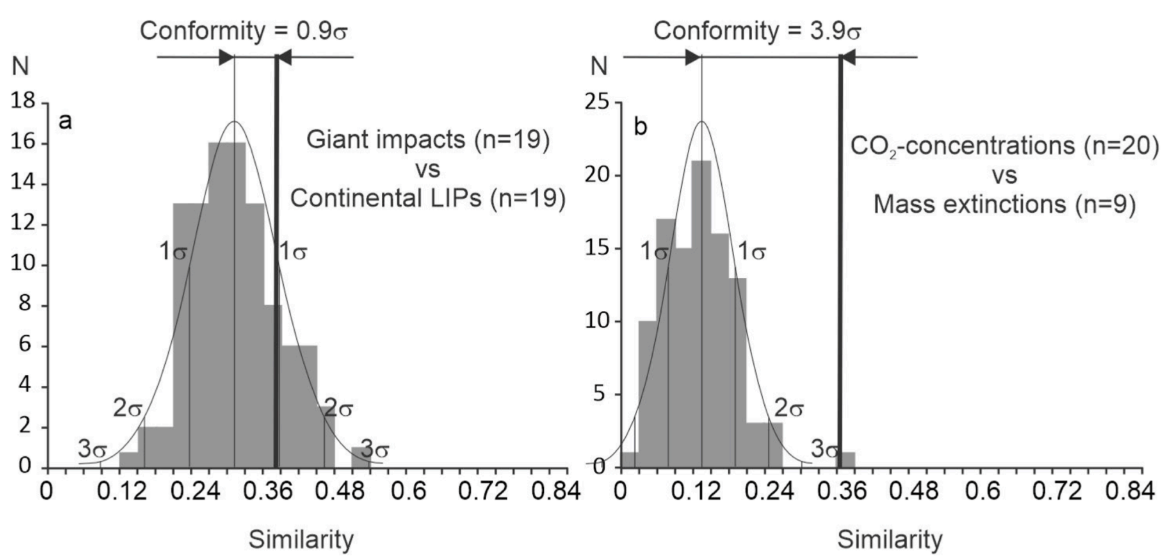

Fig. 3. The examples that illustrate the calculation of conformity metrics for two pairs of age datasets. It should be noted that these particular examples were selected for the purpose of providing a clear representation of the method from a larger number of comparisons, in which similarity coefficients ranged from 0 to 0.859 and conformity coefficients varied from −1.4σ to 5.5σ (see files in Supplement 2). As illustrated in Fig. 3, the similarity coefficients of the compared pairs are nearly identical (demonstrated by a vertical bold line). However, the probability of generating such similarity coefficients through random processes (illustrated by grey columns in the histogram and fitted by a Gaussian) differs significantly. In the example illustrated in (a), the similarity coefficient is indistinguishable from that generated by random processes. In contrast, in the example shown in (b), the mean similarity coefficient generated by Monte Carlo is lower by 3.9σ compared to the real similarity coefficient. The three-sigma rule can be used to identify matches between the ages of CO_2-concentration peaks and mass extinctions with a reasonable degree of confidence.

the name of the metric. The uncertainty of *C* is primarily influenced by the number of Monte Carlo simulations, *n*, as the square root of *n*. For instance, for 100 simulations, the uncertainty is 10 %.

The fundamental principle of this procedure is illustrated in Fig. 3. A comparison by Bhattacharyya (1943), which is known in geological literature as the similarity metric of Gehrels (2000), revealed that sample pairs of giant impacts versus continental LIPs and CO_2-concentration peaks versus mass extinctions yielded nearly identical similarity coefficients of approximately 0.36–0.38. Nevertheless, the generation of random datasets, which simulate real data, demonstrates that the similarity between giant impacts and continental LIPs is indistinguishable from that generated by Monte Carlo (Fig. 3a). The similarity coefficient between CO_2-concentration peaks and mass extinctions is 3.9σ higher than the Monte Carlo-generated similarity coefficient (Fig. 3b). This indicates that the observed similarity coefficient of 0.36 for the specified pair of ages could have been generated by chance with a probability of <0.0005. (This probability can be calculated using a Gaussian distribution, where the standard deviation (σ) can be converted to a probability using, for example, an Excel function such as Norm.S.Dist.) As the conformity value increases, the probability of the correlation between two pairs of datasets being explained by bad-luck coincidence decreases. Three-sigma rule can be employed to distinguish between reliable and questionable age matches, as is commonly done in many practical applications (Lehmann, 2013; Ogren et al., 2009; Oresic and Grdinic, 1990).

4. Databases

In light of the growing body of evidence concerning environmental catastrophes, particularly the anthropogenic global temperature rise (IPCC, 2018), there has been a notable increase in research focusing on CO_2 atmospheric concentrations (Bedrner, 1991; Cui et al., 2021;

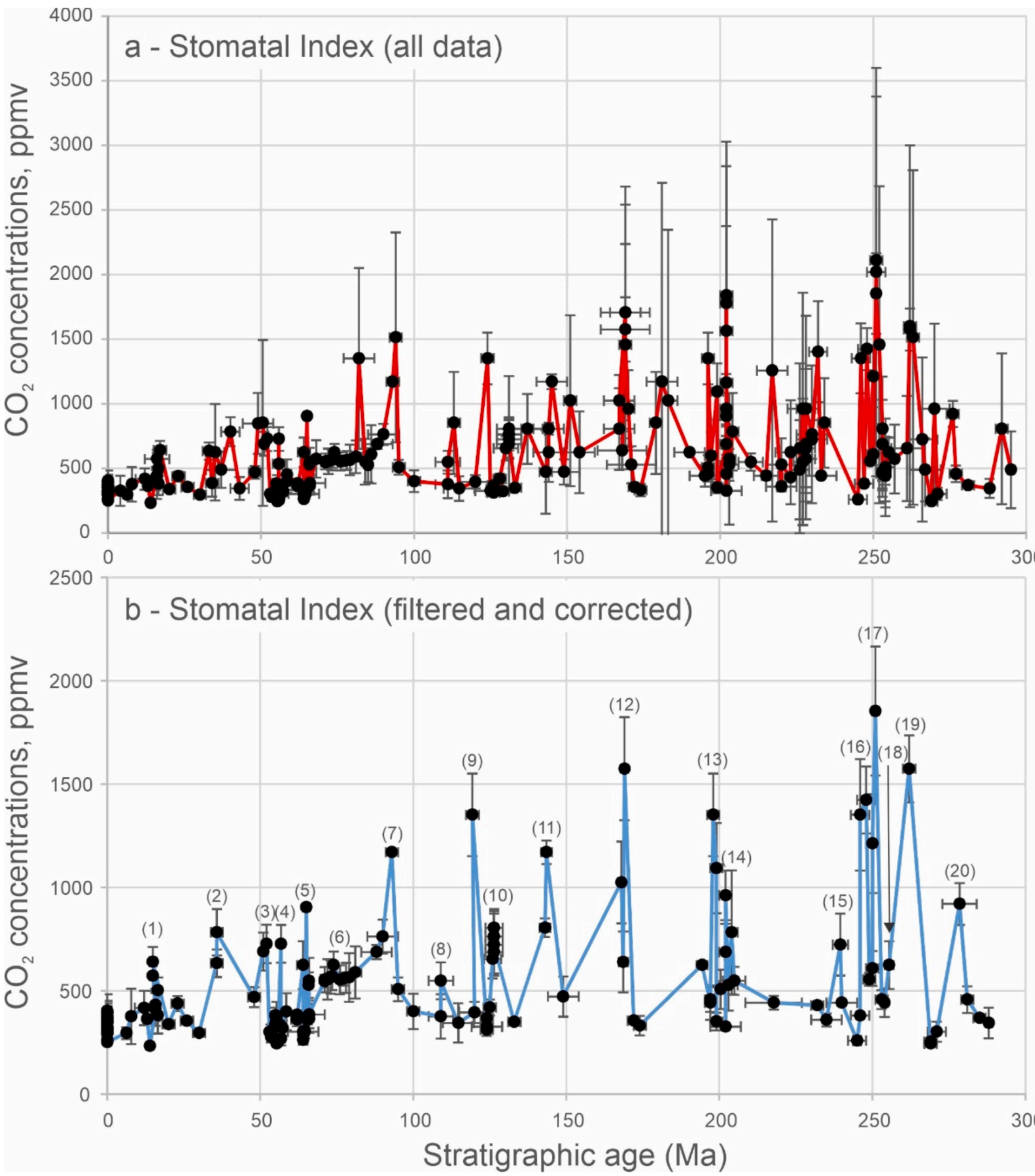

Fig. 4. (a) CO_2 concentrations calculated using the stomatal index (reproduced after Retallack and Conde, 2020), (b) the same dataset after filtering out CO_2 concentrations with uncertainty greater than 25 % and correcting ages using the latest version of the International Stratigraphic Chart (https://stratigraphy.org, v2023/09). The CO_2-concentration peaks used in the statistical analysis are numbered.

Schoepfer et al., 2022). A recent study by Retallak and Conde (2020) has proposed a robust record of CO_2 concentrations in the Earth's atmosphere over the last 300 million years. This record is based on the analysis of stomatal index in Gingko and Lepidopteris leaves, and provides a basis for testing the role of CO_2 in mass extinctions and other environmental catastrophes.

In their study, Retallack and Conde (2020) converted the stratigraphic ages of Gingko and Lepidopteris fossils to numerical age values. A plot of CO_2 stomatal index-derived atmospheric concentrations versus age reveals a number of pronounced CO_2 concentration peaks above 500 ppmv (Retallack and Conde, 2020) (Fig. 4a). Nevertheless, it should be noted that the determination of certain CO_2 concentrations was subject to a considerable degree of uncertainty. Accordingly, in the present study, the CO_2 data were subjected to a filtration process, whereby values with uncertainties exceeding 25 % were removed. A review of the tabulated age data indicates that a significant number of the stratigraphic age values presented in Retallak and Conde (2020) were derived from an outdated version of the stratigraphic scale (Table 1). Consequently, the stratigraphic ages were corrected using the most recent version of the International Stratigraphic Scale (https://stratigraphy.org, v2023/09). To illustrate, if the stomatal index was determined for a species occurring in middle Ypresian strata, the age of 51.5 ± 0.7 Ma was attributed using the ages of 56.0 Ma and 47 Ma for the Ypresian/Thanetian and Lutetian/Ypresian boundaries, respectively, on the assumption of equal duration of the early, middle and late Ypresian. In the event that the age of a stratigraphic boundary is represented with uncertainty, this is included in the calculation of the duration of the corresponding stratigraphic stage. In total, twenty CO_2-concentration peaks were identified (Fig. 4b) (Table 1). The majority of these CO_2-concentration peaks exhibit a rapid increase and subsequent decrease, with the exception of peak No. 6, which persisted for approximately ten million years at concentrations just above the specified threshold value of 500 ppmv (Fig. 4b).

In order to identify the environmental perturbations, the list of nine mass extinctions of the last 300 million years, as proposed by Bambach (2006), was utilised. Two of these are found to coincide with ocean anoxic events. Furthermore, four additional ocean anoxic events identified in the literature (Beil et al., 2020; Bottini et al., 2018; Graziano et al., 2013; Scott, 2014; Sell et al., 2014) were incorporated into the analysis. Additionally, four events of rapid temperature increase, referred to in the literature as climatic optimum and thermal highs, were incorporated (Crouch et al., 2020; Methner et al., 2020; Van der Boon et al., 2021; Westerhold et al., 2009). For each of these environmental-perturbation events, an age was assigned based on the most recent studies (Table 2).

In the field of bolide impact studies, the existing literature includes a number of compilations of impact structures. These include works by Firestone (2020), Green et al. (2022), Jourdan et al. (2012), Kenkmann (2021) and Schmieder et al. (2020). However, there are discrepancies between these compilations with regard to the number of structures included and the assigned ages. The present study makes use of the most comprehensive datasets from Schmieder et al. (2020) and Kenkmann (2021). The data were filtered to retain only ages with uncertainty better than 10 %. It became evident that there were discrepancies between the age values listed by Schmieder et al. (2020) and Kenkmann (2021) for a considerable number of the same impact events. The combined list comprises a total of 53 bolide impacts, with 77 age values (see Table 3). It is anticipated that only those impacts of a giant size have the potential to exert a global influence, resulting in mass extinctions (Walkden and Parker, 2008). For the purposes of the analysis, the bolide impacts were further separated by size, into three categories: giant (>40 km in diameter), large (18–40 km in diameter) and small impacts (<18 km in diameter). The delineations of size are somewhat arbitrary and partially based on the observation that different studies report disparate sizes for the same craters. For instance, Kenkmann (2021) cites diameters of 11 km and 85 km for the Ternovka and Chesapeake impacts, while

Table 1
A chronological dataset of CO_2-concentration peaks (filtered data after Retallack and Conde, 2020).

Peak No	Samples description	CO_2-conc., ppmv	Age, Ma	Corrected age relative ISC[α], Ma
	After Retallack and Conde (2020)			
1	*Ginkgo occidentalis*, early Langhian *Ginkgo adiantoides*, middle Miocene	572 ± 73 640 ± 71	16 ± 4 17 ± 2	[1]14.9 ± 1.08
2	*Ginkgo adiantoides*, late Priabonian *Ginkgo tatjanae*, late Eocene	633 ± 67 783 ± 112	33 ± 2 40 ± 3	[2]35.805 ± 1.905
3	*Ginkgo adiantoides*, middle Ypresian *Ginkgo adiantoides*, middle Ypresian	690 ± 92 727 ± 93	51.0 ± 0.2 52.0 ± 0.2	[3,*]51.5 ± 0.7
4	*Ginkgo cranei*, late Thanetian	727 ± 91	55.8 ± 0.2	[4]56.8 ± 0.4
5	*Ginkgo adiantoides*, middle Danian *Ginkgo wyomingensis*, early Danian *Ginkgo adiantoides*, late Maastrichtian *Ginkgo adiantoides*, late Maastrichtian	624 ± 115 904 ± 1 527 ± 62 548 ± 111	64 ± 2 65 ± 1 65.8 ± 0.2 65.9 ± 0.2	[5,**]65 ± 1
6	*Ginkgo adiantoides*, Campanian *Ginkgo adiantoides*, Campanian *Ginkgo adiantoides*, Campanian *Ginkgo adiantoides*, Campanian *Ginkgo adiantoides*, Campanian *Ginkgo adiantoides*, Campanian *Ginkgo adiantoides*, Campanian *Ginkgo adiantoides*, Campanian *Ginkgo adiantoides*, Campanian *Ginkgo adiantoides*, Campanian *Ginkgo adiantoides*, Campanian	546 ± 31 553 ± 61 555 ± 98 567 ± 81 569 ± 65 624 ± 66 553 ± 70 557 ± 32 562 ± 73 564 ± 118 589 ± 126	71 71 72 73 73.5 74 76 77 78 79 81	[6]77.85 ± 5.95
7	*Ginkgo pilifera*, early Coniacian *Ginkgo pilifera*, late Turonian *Ginkgo aff. G. pilifera*, early Turonian	687 ± 34 762 ± 82 1170 ± 0	88 ± 5 90 ± 5 93 ± 2	[7]90.7 ± 3.2
8	*Ginkgo paradiantoides*, early Albian	548 ± 89	111 ± 4	[8]109 ± 4
9	*Gingkoites australis*, early Aptian	1351 ± 200	124 ± 2	[9]119.3 ± 2.1
10	*Ginkgoites myrioneurus*, early Barremian *Ginkgoites subadiantoides*, late Hauterivian *Ginkgoites elegans*, late Hauterivian *Ginkgoites manchuricus*, late Hauterivian *Ginkgoites microphyllus*, late Hauterivian	654 ± 94 762 ± 123 805 ± 90 687 ± 103 723 ± 150	130 ± 4 131 ± 4 131 ± 4 131 ± 4 131 ± 4	[10]126.385 ± 2.8
11	*Ginkgo coriacea*, middle Berriasian *Ginkgo manchurica*, early Berriasian	805 ± 45 1170 ± 57	144 ± 5 145 ± 5	[11]143.25 ± 1.75
12	*Ginkgo huttoni*, basal Bathonian	1024 ± 198	167 ± 5	[12]168.56 ± 1.56

(*continued on next page*)

Table 1 (*continued*)

Peak No	Samples description After Retallack and Conde (2020)	CO_2-conc., ppmv	Age, Ma	Corrected age relative ISC[α], Ma
	Ginkgoites regnellii, late Bajocian	639 ± 147	168 ± 8	
	Ginkgo sibirica, middle Bajocian	1574 ± 249	169 ± 8	
13	*Ginkgo obrutschewi*, late Sinemurian	624 ± 11	190 ± 5	[13]196.2 ± 3.6
	Ginkgoites marginatus, early Sinemurian	1351 ± 200	196 ± 2	
14	*Ginkgoites marginata*, late Rhaetian	687 ± 137	202 ± 2	[14]204.85 ± 3.65
	Ginkgoites troedssoni, late Rhaetian	961 ± 120	202 ± 2	
	Ginkgoites acosmia, early Rhaetian	527 ± 123	203 ± 3	
	Lepidopteris ottonis, early Rhaetian	783 ± 300	204 ± 2	
	cf. *Lepidopteris ottonis*, early Rhaetian	548 ± 67	201 ± 4	
15	*Lepidopteris haizeri*, late Ladinian	723 ± 150	230 ± 5	[15]239.5 ± 2.5
16	*Lepidopteris madagascariensis*, early Anisian	1351 ± 270	246 ± 3	[16]246 ± 1.2
	Lepidopteris madagascariensis, early Anisian	1423 ± 162	248 ± 3	
17	*Lepidopteris callipteroides*, early Griesbachian	608 ± 84	250 ± 2	[17]251.562 ± 0.362
	Lepidopteris callipteroides, early Griesbachian	1212 ± 239	250 ± 2	
	Tatarina rinatata, early Griesbachian	1853 ± 312	251 ± 1	
18	*Tatarina mira*, late Wuchiapingian	624 ± 115	255 ± 1	[18]255.48 ± 1.41
19	*Sphenobaiera sp*, mid Capitanian	1574 ± 162	262 ± 2	[19]262 ± 2
20	*Auritifolia* sp., Kungurian	920 ± 120	276 ± 2	[20]278.485 ± 5.615

[α] According to International Stratigraphic Chart.
[1] Langhian is bounded between 15.98 and 13.82 Ma.
[2] Late Eocene consists of Priabonian, which is bounded between 37.71 and 33.9 Ma.
[3] Ypresian is bounded between 56.0 and 47.8 Ma.
[4] Thanetian is bounded between 59.2 and 56.0 Ma.
[5] Maastrichtian is bounded between 72.1 ± 0.2 and 66.0 Ma. Danian is bounded between 66.0 and 61.6 Ma.
[6] Campanian is bounded between 83.6 ± 0.2 and 72.1 ± 0.2 Ma.
[7] Turonian begins at 93.9 Ma, Coniacian ends at 86.3 ± 0.5 Ma.
[8] Albian is bounded between 113.0 and 100.5 Ma.
[9] Aptian is bounded between 121.4 and 113.0 Ma.
[10] Hauterivian is bounded between 132.6 and 125.77 Ma, Barremian is bounded between 125.77 and 121.4 Ma.
[11] Berriasian is bounded between 145.0 and 139.8 Ma.
[12] Bajocian is bounded between 170.9 ± 0.8 and 168.2 ± 1.2 Ma, and Bathonian is bounded between 168.2 ± 1.2 and 165.3 ± 1.1 Ma.
[13] Sinemurian is bounded between 199.5 ± 0.3 and 192.9 ± 0.3 Ma.
[14] Rhaetian is bounded between 208.5 and 201.4 ± 0.2 Ma.
[15] Landian is bounded between 242 and 237 Ma.
[16] Anisian is bounded between 247.2 and 242 Ma.
[17] Griesbachian is a substage of Induan, which is bounded between 251.902 ± 0.024 and 251.2 Ma.
[18] Wuchaipingian is bounded between 259.51 ± 0.21 and 254.14 ± 0.07 Ma.
[19] Capitanian is bounded between 264.28 ± 0.16 and 259.51 ± 0.21 Ma.
[20] Kungurian is bounded between 283.5 ± 0.6 and 273.01 ± 0.14.
[*] Average of estimate of Retallack and Conde (2020).
[**] CO_2-peak is set to early Danian.

Table 2
Age of prominent environmental perturbations (an updated list of Courtillot and Renne, 2003 with mass-extinctions after Bambach, 2006).

Environmental perturbations (mass extinctions – ME, ocean anoxic event – OAE, climatic optimum – CO or thermal high – TH)	Age, Ma	Key ref.
Pliocene ME	3.1 ± 0.7	[1]
Middle Miocene CO	15.83 ± 1.17	[2]
Late Eocene ME	34.09 ± 0.08	[3]
Middle Eocene CO	40.2 ± 0.3	[4]
Early Eocene CO	51.10 ± 2.06	[5]
Paleocene-Eocene TH	56.152 ± 0.141	[6]
Late Maastrichtian ME	66.00 ± 0.07	[7]
Late Cenomanian OAE2 and ME	94.17 ± 0.17	[8]
OAE1d	97.6 ± 0.2	[9]
OAE1c	101.9 ± 0.5	[9]
OAE1b	111.17 ± 0.92	[9]
Selli OAE1a	123.855 ± 0.695	[10]
Weissert OAE	133.2 ± 0.6	[11]
Late Tithonian ME	146.8 ± 1.3	[12]
Toarcian OAE and late Pliensbachian/early Toarcian ME	182.605 ± 0.76	[13]
Late Norian/Rhaetian ME	201.564 ± 0.015	[14]
Changhsingian ME	251.97 ± 0.06	[15]
Capitanian ME	260.5 ± 0.3	[16]

References: [1] Pimiento et al. (2017); [2] Methner et al. (2020); [3] Sahy et al. (2020); [4] Van der Boon et al. (2021); [5] Crouch et al. (2020); [6] Westerhold et al. (2009); [7] Husson et al. (2011); [8] Beil et al. (2020); [9] Scott (2014); [10] Graziano et al. (2013); [11] Bottini et al. (2018); [12] Bambach (2006); [13] Sell et al. (2014); [14] Blackburn et al. (2013); [15] Burgess et al. (2014); [16] Day and Rubidge (2021).

Schmieder et al. (2020) cite diameters of 17.5 km and 40 km (Table 3). The discrepancy between the two size categories, particularly for the giant Chesapeake impact, can be attributed to the fact that the larger size was an observed value, whereas the smaller size was inferred from modelling, taking into account anomalously shallow crater depth for the observed crater size (Walkden and Parker, 2008).

Large Igneous Provinces (LIPs) represent anomalous volumes of volcanic activity. Nevertheless, the precise definition of LIP remains unclear. The most commonly used definition is that proposed by Bryan and Ernst (2008). Accordingly, the list of LIPs was derived from Ernst's compilation (2014; http://www.largeigneousprovinces.org), which employs a ranking system categorising LIPs as A, B, or C based on the significance of volcanism. The statistical analysis was conducted using only those LIPs that had been ranked as A or B. For each LIP, a literature search was conducted with the objective of updating the age information, as presented in Table 4. A comprehensive compilation of U-Pb and $^{40}Ar/^{39}Ar$ ages has recently been provided by Jiang et al. (2023). However, this comprises a smaller number of individual or grouped LIPs than the list provided by Ernst (2014; http://www.largeigneousprovinces.org). Table 5 also presents the mean ± one standard deviation of the "filtered robust and precise" ages provided by Jiang et al. (2023) for each LIP. It is evident that even these ages exhibit a considerable degree of variation when compared to the results of comprehensive studies on specific LIPs. For example, Ivanov et al. (2017) demonstrated that U-Pb ages obtained by ID-TIMS on zircon and baddeleyite single grains yielded a considerably narrower time span for the duration of the Karoo-Ferrar volcanism than other variants of U-Pb dating or $^{40}Ar/^{39}Ar$ methods. Therefore, age of the Karoo-Ferrrar LIP based on Ivanov et al. (2017) and Jiang et al. (2023) studies are respectively 182.5 ± 0.5 Ma (where uncertainty is the maximal duration of the most voluminous phase of volcanism) and 182.0 ± 2.0 Ma (where uncertainty is one σ of the filtered "robust and precise" age determinations by all analytical methods). Similarly, for the Siberian Traps, based on U-Pb ID-TIMS data,

Table 3
Ages of bolide impacts determined with precision of better than 10 % and impact crater diameters (combined after Schmieder et al., 2020 and Kenkmann, 2021).

Name	Diameter, km	Age, Ma
Small impacts (0–18 km diameter crater)		
Kamil	0.045 [k]	0.00302 ± 0.0006 [k]
Kaalijarv	0.11 [k]	0.00351 ± 0.00004 [k]
Macha	0.3 [k,s]	0.007315 ± 0.00008 [k,s]
Haviland	0.015[s], 0.017 [k]	0.02 ± 0.002 [k,s]
Xiuyan	1.8 [k]	0.050 ± 0.005 [k]
Barringer	1.186 [s]	0.0611 ± 0.0048 [s]
Odessa	0.168[s], 0.17 [k]	0.0635 ± 0.0045 [k,s]
Wolfe Creek	0.875[s], 0.88 [k]	0.12 ± 0.009 [k,s]
Lonar	1.83[s], 1.88 [k]	0.570 ± 0.047 [k], 0.576 ± 0.047 [s]
Pantasma	14 [k,s]	0.815 ± 0.011 [k,s]
Bosumtwi	10.5 [s]	1.13 ± 0.1 [s]
New Quebec	3.4 [k], 3.44 [s]	1.4 ± 0.1 [k,s]
Tenoumer	1.9 [k,s]	1.52 ± 0.14 [k], 1.57 ± 0.14 [s]
Aouelloul	0.36[s], 0.39 [k]	3.1 ± 0.3 [k,s]
Roter Kamm	2.5 [s]	3.8 ± 0.3 [s]
Libian desert	No crater	29 ± 1 [k]
Wanapitei	7.5 [k,s]	37 ± 2 [k], 37.7 ± 1.2 [s]
Gusev	3 [k]	50.36 ± 0.33 [k]
Marguez	13[s], 15 [k]	58.3 ± 3.1 [k,s]
Wetumpka	7 [k]	84.4 ± 1.4 [k]
Mien	9 [k,s]	118.7 ± 2.3 [k], 122.4 ± 2.3 [s]
Vargeao	12 [s]	123 ± 1.4 [s]
Yepriaj	8[s, k]	160 ± 5 [s]
Ramgarh	10.2 [k]	164.8 ± 1.3 [k]
Zapadnaya	3.2 [k,s]	165 ± 5 [k], 165 ± 6 [s]
Gow Lake	5 [s]	196.8 ± 9.9 [s]
Paasselka	10 [k,s]	228.7 ± 3.0 [k], 231 ± 2.2 [s]
Ternovka	11 [k], 17.5 [s]	280 ± 10 [k,s]
Large impacts (18–40 km diameter crater)		
El`gygytgyn	18 [k,s]	3.58 ± 0.04 [k], 3.65 ± 0.08 [s]
Ries	24 [s]	14.808 ± 0.038 [s]
Haughton	24 [s]	23.4 ± 1 [s]
Logoisk	17 [k,s]	29.71 ± 0.48 [k], 30 ± 0.5 [s]
Mistastin	28 [k,s]	36.6 ± 2 [k], 37.83 ± 0.05 [s]
Kamensk	25 [k,s]	50.36 ± 0.33 [k], 50.37 ± 0.4 [s]
Boltysh	24 [k,s]	65.17 ± 0.64 [k], 65.8 ± 0.67 [s]
Manson	35 [k,s]	74.1 ± 0.1 [k], 75.9 ± 0.1 [s]
Lappajarvy	23 [k,s]	77.80 ± 0.78 [k], 77.85 ± 0.78 [s]
Steen River	25 [s]	132 ± 1.3 [s]
Dellen	19[s], 20 [k]	140.82 ± 0.51 [k,s]
Mjolnir	30[s], 40 [k]	142.0 ± 2.6 [k], 143 ± 2 [s]
Obolon`	20 [s]	169 ± 7 [s]
Rochechouart	23 [k], 24.5 [s]	201 ± 2 [k], 206.92 ± 0.32 [s]
West Clearwater Lake	36 [s]	286.2 ± 2.6 [s]
Giant impacts (>40 km diameter crater)		
Chesapeake	40[s], 85 [k]	34.86 ± 0.36[s], 35.2 ± 0.3 [k]
Popigai	100 [k,s]	35.7 ± 0.2 [k], 36.63 ± 0.92 [s]
Montagnais	45 [k,s]	50.5 ± 0.8 [k], 51.1 ± 1.6 [s]
Chicxulub	180 [k,s]	66.052 ± 0.043 [s]
Kara	65 [k,s]	70.3 ± 2.2 [k], 70.7 ± 2.2 [s]
Tookoonooka	55[s], 66 [k]	125 ± 1[s], 128 ± 5 [k]
Morokweng	70 [k,s]	145 ± 2 [k], 146.06 ± 0.16[s]
Manicouagan	100 [s]	215.56 ± 0.05 [s]
Lake Saint Martin	40 [k,s]	227.4 ± 0.8 [k], 227.8 ± 0.9 [s]
Araguainha	40 [s]	254.7 ± 2.5[s], 259 ± 5[s], 251.5 ± 2.9 [s]

Source of data: [s] - Schmieder et al. (2020), [k] - Kenkmann, 2021. [k,s] – means that the same value is listed in both sources.

Ivanov et al. (2021) propose a duration of 1.91 ± 0.38 million years for the most voluminous phase, whereas the duration based on the compilation of Jiang et al. (2023) suggests a significantly longer period of 5.2 million years. A comparison of the LIP ages from the two datasets is presented in Supplement 3 (Fig. S1). It can be observed that all ages fall within the stated ranges. In the statistical analysis, the dataset with the lowest level of uncertainty, as derived from Ernst's list (Table 4), is employed.

Table 4
Age of large igneous provinces (LIPs).

LIPs[a]	C – continental, O –oceanic	Age, Ma (this study)	Key ref.	Age, Ma (Jiang et al., 2023)
[b] **Columbia River**	C	16.3 ± 0.4	[1]	16.3 ± 0.4
Afar	C	30 ± 1	[2]	28.8 ± 3.8
[c] Neotethys	C	40 ± 4	[3]	
North Atlantic volcanic province 2	C	55.6 ± 2	[4]	55.6 ± 6.8
North Atlantic volcanic province 1	C	59.5 ± 3.5	[4]	
Deccan	C	66.0 ± 0.4	[5]	66.0 ± 0.7
Carmacks	O	70.5 ± 1.5	[6]	
Maud Rise, Sierra Leone Rise	O	73 ± 1	[7]	
Carribian-Colombian, Madagascar, Sarnu-Dandali,	C & O	88.5 ± 2.5	[8]	88.7 ± 15.1 90.7 ± 1.5
Ontong Java 2, Manihiki Plateau 2	O	93 ± 6	[9]	99.2 ± 7.2
Queen Elizabeth Islands, Alpha Ridge, Wallaby Plateau	C & O	95.5 ± 0.5	[10]	
Naturaliste Plateau	O	101 ± 1	[11]	
Kerguelen, Marie Byrd Land, Hikurangi Plateau, Hess Rise, Nauru Basin	C & O	107 ± 5	[12]	109.8 ± 12.7
Rajmahal-Sylhet	C	114.5 ± 1.5	[13]	
Magellan Rise	O	118.2 ± 1.2	[14]	
Ontong-Java 1, Manihiki Plateau, Pinon Formation	O	124 ± 2	[15]	126.3 ± 0.9
Paraná-Etendeka	C	133.5 ± 1.5	[16]	133.5 ± 3.7
Gascoyne Margin	C	132 ± 1	[17]	
Trap, SW Greenland	C	135.5 ± 2.5	[18]	
Shatsky Rise	O	?	[19]	
Sorachi event	O	151.1 ± 6.1	[20]	
Argo Basin	O	165.5 ± 1.5	[21]	
Karoo-Ferrar	C	182.5 ± 0.5	[22]	182.0 ± 2.0
Central Atlantic Magmatic Province	C	201.35 ± 0.35	[23]	200.9 ± 1.9
Angayucham	O	?	[24]	
Wrangellia	O	232.2 ± 1.0	[25]	
Siberian Traps	C	251.3 ± 1.0	[26]	250.6 ± 5.2
Emeishan	C	260.1 ± 1.2	[27]	258.3 ± 3.3
Cache Creek	O	263.1 ± 1.4	[28]	
Panjal Traps	C	285 ± 1	[29]	
Tarim	C	287.0 ± 2.5	[30]	277.8 ± 7.8

Note.
[1] Kasbohm and Schoene (2018); [2] Baker et al. (1996); [3] Van der Boon et al. (2021); [4] http://www.largeigneousprovinces.org/16dec; [5] Schoene et al. (2019); [6] Johnston et al. (1996); [7] Eldholm and Coffin (2000); [8] Kerr et al. (1997); Sheth et al. (2017); Storey et al. (1995); [9] Eldholm and Coffin (2000); Hoernle et al. (2010); [10] Eldholm and Coffin (2000); Embry and Osadetz (1988); Tarduno et al. (1998); [11] Eldholm and Coffin (2000); [12] Eldholm and Coffin (2000); Neal et al. (1997); Storey et al. (1999); [13] Kent et al. (1997); [14] Koppers et al. (2000); [15] Eldholm and Coffin (2000); Hoernle et al. (2010); Lapierre et al. (2000); Parkinson et al. (2002); [16] Gomes et al. (2021); [17] Rey et al. (2008); [18] Larsen et al. (1999); [19] Eldholm and Coffin

(2000); [20] Takashima et al. (2006); [21] Rey et al. (2008); [22] Ivanov et al. (2017); [23] Devies et al. (2017); [24] Pallister et al. (1989); [25] Mortensen et al. (1992); [26] Burgess and Bowring (2015); Ivanov et al. (2021); [27] Li et al. (2018); [28] Mihalynuk et al. (1997); [29] Dan et al. (2021); [30] Zhong et al. (2021).

[a] – list after http://www.largeigneousprovinces.org/record.

[b] – bold names are for those that are in both databases (Ernst's and Jiang et al., 2023).

[c] – not in the original Ernst's list.

Table 5
Assessment of the age matching by statistical test using conformity (*C*) metric.

Pair of datasets for comparison[1]	*x(S)*	<*x*> *(SS)* ± *σ(SS)*	*C* ± *se*	Probability of bad-luck coincidence
Test comparison for datasets whose ages are matched by default				
OAE vs ME	**0.305**	**0.042 ± 0.066**	**3.97 ± 0.40**	**0.00035**
Giant impacts vs all impacts	**0. 741**	**0.420 ± 0.089**	**3.59 ± 0.36**	**0.0012**
LIPs (Ernst) vs LIPs (Jiang et al., 2023)	**0.762**	**0.523 ± 0.066**	**3.61 ± 0.36**	**0.0011**
Potential cause vs consequence				
Continental LIPs vs *Climatic optima and thermal high*	0.286	0.116 ± 0.073	*2.35 ±* 0.23	*0.035*
Continental LIPs vs Mass extinctions	**0.447**	**0.120 ± 0.062**	**5.30 ± 0.53**	**0.0000018**
Continental LIPs vs *Ocean anoxic events*	*0.308*	*0.143 ± 0.065*	*2.55 ± 0.26*	*0.022*
Continental LIPs vs CO_2-concentration peaks	0.519	0.401 ± 0.080	1.48 ± 0.15	0.18
Oceanic LIPs vs Climatic optima and thermal high	0.000[2]			
Oceanic LIPs vs Mass extinctions	0.123	0.125 ± 0.088	−0.02 ± 0.00	1
Oceanic LIPs vs Ocean anoxic events	0.290	0.140 ± 0.081	1.86 ± 0.19	0.095
Oceanic LIPs vs CO_2-concentration peaks	0.486	0.398 ± 0.087	1.01 ± 0.10	0.36
CO_2-concentration peaks vs Climatic optima and thermal high	0.265	0.161 ± 0.087	1.20 ± 0.12	0.28
CO_2-concentration peaks vs Ocean anoxic events	0.175	0.161 ± 0.064	0.21 ± 0.02	0.85
CO_2-concentration peaks vs Mass-extinctions	**0.363**	**0.132 ± 0.060**	**3.87 ± 0.39**	**0.00049**
Giant impacts vs Continental LIPs	0.381	0.313 ± 0.074	0.92 ± 0.09	0.41
Giant impacts vs Oceanic LIPs	0.323	0.298 ± 0.077	0.32 ± 0.03	0.77
Giant impacts vs Climatic optima and thermal high	0.163	0.115 ± 0.071	0.68 ± 0.07	0.54
Giant impacts vs Mass extinctions	**0.649**	**0.114 ± 0.071**	**7.52 ± 0.75**	**< 10^{-13}**
Giant impacts vs Oceanic anoxic events	0.114	0.113 ± 0.065	0.02 ± 0.00	0.99
Giant impacts vs CO_2-concentration *peaks*	*0.558*	*0.367 ± 0.066*	*2.92 ± 0.29*	*0.0085*
Large impacts vs Climatic optima and thermal high	0.108	0.108 ± 0.075	0.01 ± 0.00	1
Large impacts vs Mass extinctions	0.241	0.109 ± 0.070	1.90 ± 0.19	0.087
Large impacts vs Oceanic anoxic events	0.071	0.122 ± 0.066	−0.77 ± *0.08*	1
Large impacts vs CO_2-concentration peaks	0.422	0.342 ± 0.070	1.14 ± 0.11	0.31

Note.
[1] Bold font is to highlight pairs whose age matching was not due to bad-luck coincidence ($C > 3σ$). Normal font – for the cases of high possibility of random coincidence ($C < 2σ$). Italic font – for those cases when interpretation is uncertain ($C = 2–3σ$).
[2] Other parameters are not calculated because of $x(S) = 0$.

5. Results

5.1. Testing the conformity metric

Let us consider datasets that are subsets of larger datasets. Among the prominent environmental perturbations, some of the ocean anoxic events can be classified as mass extinction events (see Table 2). The giant impact list is a subset of the list of impacts (see Table 3). Furthermore, the list of the LIPs of Jiang et al. (2023) partially overlaps with that of Ernst (see Table 4). The calculation of similarity and conformity for these pairs yields the following results: 0.305 and 3.97 ± 0.40σ, 0.741 and 3.59 ± 0.36σ, and 0.762 and 3.61 ± 0.36σ, respectively (Table 5). Notwithstanding the discrepancies in similarity, all three examples demonstrate conformity that can be interpreted as evidence that correlations between the compared datasets are unlikely to have occurred by bad-luck coincidence. The opposite example, comprising subsets of oceanic LIPs and climatic optima and thermal highs, exhibits no overlap in age (see Tables 2 and 4). Consequently, the similarity score is zero, and a Monte Carlo analysis is unnecessary to ascertain the absence of correlation between these two input parameters.

5.2. Conformity between potential causes and effects

This section addresses the issue of conformity with regard to potential cause-and-effect relationships. The results are presented in Table 5. The conformity metric indicates that among the potential cause-and-effect pairs under consideration, only a small number could not be deemed to have originated as a result of a bad-luck coincidence. These are evident age correlations between continental LIPs and mass extinctions, bolide impacts and mass extinctions, and CO_2-concentration peaks and mass extinctions. These pairs of age datasets are distinguished by a conformity exceeding 3σ, with the highest conformity value (7.5σ) observed between giant bolide impacts and mass extinctions (Table 5). Some age pairs exhibit conformity between 2σ and 3σ, thereby leaving uncertainty in the interpretation of their age matching by random or non-random processes. These include continental LIPs and climatic optima and thermal highs, as well as continental LIPs and ocean anoxic events, and giant impacts and CO_2-concentration peaks. The conformity between bolide impacts (either large or giant) and LIPs, between LIPs and CO_2-concentration peaks, and between bolide impacts and CO_2-concentration peaks is low, indicating the absence of a cause-and-effect relationship between these pairs.

6. Discussion

There is compelling evidence that the ages of mass extinctions correlate with giant bolide impacts (see Table 5). The extent of the influence of a bolide impact event on the surrounding environment is likely to be contingent upon the size of the projectile, which can be estimated from the diameter of the crater in the first instance. In consideration of giant bolide impacts, there are ten dated craters with a diameter exceeding 40 km, with 19 potential ages identified (Table 3). It can be observed that the Chicxulub, Morokweng and Araguainha craters have ages that coincide with the Late Maastrichtian (at ~66 Ma), Late Tithonian (at ~147 Ma) and Changhsingian (at ~252 Ma) mass extinctions, respectively (Tables 2 and 3). The consistency of the data demonstrates that the matching of the ages of giant bolide impacts and mass extinctions with the stated uncertainties and within the time interval of the latest 300 million years is not a bad-luck coincidence. Of the 15 dated large bolide impacts (18–40 km diameter craters), the El'gygytgyn and Boltysh craters align with the Pliocene (at ~ 3 Ma) and Late Maastrichtian (at ~66 Ma) mass extinctions, respectively (Tables 2 and 3). However, the observed conformity (1.90 ± 0.19σ) between these impacts and the mass extinctions raises questions about the likelihood of bolide impacts of that size being the primary cause of mass extinction events.

The ages of continental LIPs are found to correspond with those of mass extinctions, with a conformity of 5.30 ± 0.53σ, thereby indicating that these age matches are not coincidental (Table 5). A review of Ernst's database revealed that five of the 19 listed continental LIPs correspond with mass extinctions. Specifically, the Late Maastrichtian (at ~66 Ma), late Pliensbachian/early Toarcian (at ~182.5 Ma), Late Norian/Rhaetian (at ~201.5 Ma), Changhsingian (at ~252 Ma) and Capitanian (at ~260.5 Ma) mass extinctions occurred during the formation of the Deccan Traps, the Karoo-Ferrar Traps, the Central Atlantic Magmatic Province, the Siberian Traps and the Emeishan Traps, respectively (see Tables 2 and 4). The conformity metric indicates that there is insufficient evidence to determine whether continental LIPs were the cause of ocean anoxic events or played a role in establishing climatic optima and thermal highs.

The ages of CO_2-concentration peaks are found to align with those of mass extinctions, with a conformity of 3.87 ± 0.39σ (Table 5). A total of five of the twenty CO_2-concentration peaks exhibit overlap with mass extinctions. These include peaks No. 2, 5, 14, 17 and 19, which respectively correspond to the Late Eocene (at ~34 Ma), Late Maastrichtian (at ~66 Ma), Late Norian/Rhaetian (at ~201.5 Ma), Changhsingian (at ~252 Ma) and Capitanian (at ~260.5 Ma) mass extinctions (see Tables 1 and 2).

Of the nine mass extinction events suggested by Bambach (2006), only the Late Cenomanian (at ~94 Ma) did not overlap in age with any of the accurately dated bolide impacts, continental LIPs or CO_2-concentration peaks. Nevertheless, it is in close proximity in terms of age to CO_2-concentration peak No. 7 (Table 1). It is important to highlight that the Late Cenomanian mass extinction is distinct from other mass extinctions. For example, Smith et al. (2001) proposed that it should be considered a taphonomic megabias, defined as a product of sampling bias resulting from ocean-level rise and a shift towards deeper-water facies in the rock record. In other words, the Late Cenomanian mass extinction is not a true extinction event, unlike other cases. The Pliocene mass extinction, with only approximately 8 % of genus extinction overlaps by age with the 18 km-diameter El'gygytgyn crater, is an example of a different scenario. However, the low conformity between bolide impacts of such size and mass extinction suggests that this overlap could be coincidental.

The most severe mass extinctions are the Late Maastrichtian (at ~66 Ma, commonly referred to as KT – Cretaceous-Paleogene) and the Changhsingian (at ~252 Ma, commonly referred to as PT – Permian-Triassic). These extinctions resulted in a significant transformation in the nature of marine faunas (Bambach, 2006, 148 p.). The two mass extinctions in question overlap in age with three potential causes: giant bolide impact, continental LIP and CO_2-concentration peak (see Fig. 5). It should be noted, however, that the age of the Araguainha impact has not been accurately determined. The literature presents three different ages for the crater (Schmieder et al., 2020; Table 4). For example, Ivanov et al. (2013) argued that a bolide impact could not have occurred at the Permo-Triassic boundary, given that sediments of this age exhibit no elevated concentrations of platinum group elements (Brookfield et al., 2010). It is also important to note that the extinction of marine fauna during the Changhsingian period was a rapid event, whereas the extinction of terrestrial plants began in high latitudes and ended later in the tropics, spanning a duration of nearly one million years (Davydov et al., 2021; Wu et al., 2024). As a hypothesis, one may suggest that the rapid marine extinction coincided with the bolide impact and the terrestrial extinction, which may have been caused by prolonged volcanism. Another topic open to debate is the occurrence of anomalous volcanic events of short duration within LIPs, which may have been responsible for marine faunal extinction (Burgess et al., 2017; Sobolev et al., 2011). To illustrate, the most voluminous phase of the Siberian Traps LIP is estimated to have lasted approximately two million years (Ivanov et al., 2021). However, the volcanic eruptions that occurred during this period were relatively short-lived of order of ten thousand years, with most of the time characterised by volcanic calms (Pavlov et al., 2019).

The next most severe mass extinctions are those of the Capitanian (at ~260.5 Ma) and the late Norian/Rhaetian (at ~201.5 Ma) periods. These events are characterised by the extinction of over 40 % of genera (Bambach, 2006). They have been linked to two potential causes: volcanism of continental LIPs and CO_2-concentration peaks. Other events with an extinction of 20 % or less of genera have been linked to only one of these potential causes: either bolide impact or continental LIP or CO_2-concentration peak (Fig. 5).

The volcanism of the Karoo-Ferrar LIP alone was responsible for the late Pliensbachian/early Toarcian mass extinction, which occurred at approximately 182.5 Ma. This event resulted in the extinction of approximately 18 % of genus species. In contrast, the volcanism of LIPs that occurred concurrently with documented rises in CO_2 concentrations

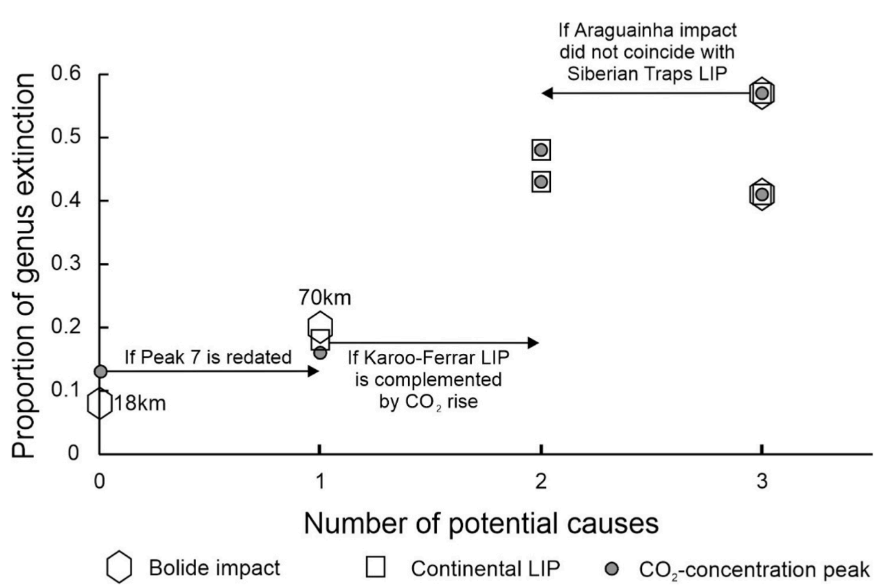

Fig. 5. Dependence of severity of mass extinction on the number of potential causes (bolide impacts, volcanism of continental LIPs, CO_2-concentration peaks). The proportion of genus extinction is based on the findings of Bambach (2006), while the number of causes is derived from this study. The arrows indicate the potential direction of change in the number of causes after the verification of data in future studies.

led to mass extinctions with a greater than 40 % extinction rate of genus species (Fig. 5). It should be noted, however, that the latter conclusion requires verification due to the lack of precise stomatal-index data at the time of the Karoo-Ferrar volcanism (Fig. 4). With additional CO_2 data, the late Pliensbachian/early Toarcian mass extinction may be reclassified as a two-cause-related mass extinction. If this is the case, it will not significantly alter the general trend illustrated in Fig. 5.

A comparison of the severity of mass extinctions with the size of bolide impact craters or the level of CO_2 concentration rise reveals no correlation (Tables 1 and 3). The volume of continental LIPs is a challenging variable to utilise in such an analysis, primarily due to the fact that a considerable proportion of these LIPs have been eroded, resulting in significant uncertainty surrounding their estimated volume. This study illustrates that the primary factor controlling the severity of mass extinctions is the interaction of multiple effects, including giant bolide impacts, volcanism associated with continental LIPs, and CO_2-concentration peaks (Fig. 5).

The statistical analysis of this study also indicates that bolide impacts did not play a significant role in the volcanism of continental LIPs, contrary to the suggestions put forth by Renne et al. (2015) and Richards et al. (2015). This is exemplified by the observation of a peaked volume of eruptions at the Deccan Traps. While there is no doubt that the Chicxulub impact occurred at the time of the Deccan volcanism, the eruptions commenced prior to and continued after the impact, thereby negating any causal connection (Mittal et al., 2022). The inability of bolide impacts to initiate volcanism was previously proposed by Ivanov and Melosh (2003). The statistical analysis of this study also demonstrated that there is no evidence that CO_2-concentration peaks were generated by volcanism. However, there is a possibility that following giant bolide impacts, there were periods of CO_2 concentration rise. Nevertheless, it is likely that the three causes of mass extinctions – bolide impacts, volcanism of continental LIPs and CO_2 concentration peaks in the atmosphere – were independent of each other. Their co-occurrence in time was unfortunate for Earth inhabitants.

It should be noted that the existence of a correlation does not necessarily imply a causal relationship. All correlations should be subjected to rigorous testing from the perspective of physical and biological mechanisms, particularly within the context of geological and paleogeographic factors. One might, for instance, inquire as to why a specific volcanic event led to a particular mass extinction, while others did not. However, the scope of this paper does not extend to the specifics of such a test. This is a topic that warrants further investigation in future studies.

7. Conclusions

It has been demonstrated that the conventional analysis of age matching of potential causes and consequences, when picked up ages are plotted in an age-versus-age diagram, may result in the generation of misleading results. The selection of the most appropriate age inevitably results in a one-to-one correlation.

A novel approach to age matching is proposed, wherein conventional statistical metrics are evaluated in the context of Monte Carlo-generated datasets that emulate the age distribution observed in real data. This procedure, which bears resemblance to conformity assessment (ISO/IEC 17043:2023), is henceforth referred to as the conformity metric.

The conformity metric was applied to the available and updated geochronological datasets of bolide impacts, LIPs, CO_2-concentration peaks in the atmosphere, mass extinctions, ocean anoxic events, and climatic optima and thermal highs. It has been demonstrated that mass extinctions align with the ages of their potential causes, including giant bolide impacts (crater diameter exceeding 40 km), volcanism of continental LIPs, and CO_2-concentration peaks in the atmosphere. Other potential cause-versus-consequence pairs do not exhibit a correlation.

The severity of mass extinctions is contingent upon the number of simultaneous causal factors. Two of the most severe mass extinctions, the Late Maastrichtian (~66 Ma) and the Changhsingian (~252 Ma), were likely caused by the simultaneous occurrence of volcanism of continental LIPs, giant bolide impacts and CO_2-concentration peaks in the atmosphere. Conversely, the ages of LIPs, bolide impacts and CO_2-concentration peaks do not correspond, indicating that these three causes were not interdependent.

CRediT authorship contribution statement

Alexei V. Ivanov: Writing – review & editing, Writing – original draft, Methodology, Investigation, Formal analysis, Data curation, Conceptualization.

Declaration of competing interest

The author has no competing interests.

Data availability

All data are provided within m/s and supplementary files

Acknowledgements

The author would like to acknowledge the contributions of Bruce R. Julian and Gillian R. Foulger, who provided informal comments and suggestions, as well as the two anonymous reviewers whose comments and critiques were invaluable. Alex Webb also deserves recognition for his editorial handling. One of the two reviewers was kind enough to provide MATLAB code for calculation purposes (Supplement 4). This research was conducted at the Centre for Geodynamics and Geochronology of the Institute of the Earth's Crust. The original English text underwent proofreading using DeepL artificial intelligence. Artistic figure of the graphical abstract was created using Kandinsky artificial intelligence.

Supplementary materials

Supplementary material associated with this article can be found, in the online version, at doi:10.1016/j.epsl.2024.119058.

References

Alvarez, L.W., Alvarez, W., Asaro, F., Michel, H.V., 1980. Extraterrestrial cause for the cretaceous-tertiary extinction. Science 208, 1095–1108.
Baker, J., Snee, L., Menzies, M., 1996. A brief Oligocene period of flood volcanism in Yemen: implications for the duration and rate of continental flood volcanism at the Afro-Arabian triple junction. Earth Planet. Sci. Lett. 138, 39–55.
Bambach, R.K., 2006. Phanerozoic biodiversity mass extinctions. Ann. Rev. Earth Planet. Sci. 34, 127–155.
Beil, S., Kuhnt, W., Holbourn, A., Scholz, F., Oxmann, J., Wallmann, K., Lorenzen, J., Aquit, M., Chellai, E.H., 2020. Cretaceous oceanic anoxic events prolonged by phosphorous cycle feedbacks. Clim. Past 16, 757–782.
Berner, R.A., 1991. A model for atmospheric CO2 over Phanerozoic time. Am. J. Sci. 291, 339–376.
Bhattacharyya, A., 1943. On a measure of divergence between two statistical populations defined by their probability distributions. Bull. Calcutta Math. Soc. 35, 99–109.
Blackburn, T.J., Olsen, P.E., Bowring, S.A., McLean, N.M., Kent, D.V., Puffer, J., McHone, G., Rasbury, E.T., Et-Touchami, M., 2013. Zircon U-Pb geochronology links the end-Triassic extinction with the Central Atlantic magmatic province. Science 340, 941–945.
Bottini, C., Dieni, I., Erba, E., Massari, F., Weissert, H., 2018. The Valangian Weissert oceanic anoxic event recorded in Central-Eastern Sardinia (Italy). Rev. Ital. Paleont. Stratig. 124, 617–637.
Brookfield, M.E., Shellnutt, J.G., Qi, L., Hannigan, R., Bhat, G.M., Wignall, P.B., 2010. Platinum element group variations at the Permo-Triassic boundary in Kashmir and British Columbia and their significance. Chem. Geol. 272, 12–19.
Bryan, S.E., Ernst, R.E., 2008. Revised definition of large igneous provinces (LIPs). Earth Sci. Rev. 86, 175–202.
Burgess, S.D., Bowring, S., 2015. High-precision geochronology confirms voluminous magmatism before, during, and after Earth's most sever extinction. Sci. Adv. 1. https://doi.org/10.1126/sciadv.1500470.
Burgess, S.D., Bowring, S., Shen, S.-Z., 2014. High-precision timeline for Earth's most sever extinction. Proc. Natl. Acad. Sci. 111, 3316–3321.

Burgess, S.D., Muirhead, J.D., Bowring, S.A., 2017. Initial pulse of Siberian Traps sills as the trigger of the end-Permian mass extinction. Nat. Commun. 8, 164.

Courtillot, V.E., Renne, P.R., 2003. On the age of flood basalt events. Compt. Ren. Geosci. 335, 113–140.

Crouch, E.M., Shepherd, C.L., Morgans, H.E.G., Naafs, B.D.A., Dallanave, E., Phillips, A., Hollis, C.J., Pancost, R.D., 2020. Climatic and environmental changes across the early Eocene climatic optimum at mid-Waipara River, Canterbury Basin, New Zealand. Earth-Sci. Rev. 200, 102961.

Cramer, H., 1946. Mathematical Methods of Statistics. Princeton University Press, Princeton, New Jersey.

Cui, Y., Li, M., Van Soelen, E.E., Kurschner, W.M., 2021. Massive and rapid predominantly volcanic CO_2 emission during the end-Permian mass extinction. Proc. Natl. Acad. Sci. 118, e2014701118.

Dan, W., Wang, Q., Murphy, J.B., Zhang, X.-Z., Xu, Y.-G., White, W.M., Jiang, Z.-Q., Hao, L.-L., Qi, Y., 2021. Short duration of early Permian Qiangtang-Panjal large igneous province: implications for origin of Neo-Tethys Ocean. Earth Planet. Sci. Lett. 568, 117054.

Davies, J.H.F.L., Marzoli, A., Bertrand, H., Youbi, N., Ernesto, M., Schaltegger, U., 2017. End-Triassic mass extinction started by intrusive CAMP activity. Nat. Comm. 8, 15596.

Davydov, V.I., Karasev, E.V., Nurgalieva, N.G., Schmitz, M.D., Budnikov, I.V., Biakov, A. S., Kuzina, D.M., Silantiev, V.V., Urazaeva, M.N., Zharinova, V.V., Zorina, S.O., Gareev, B., Vasilenko, D.V., 2021. Climate and biotic evolution during the Permian-Triassic transition in the temperate Northern Hemisphere, Kuznetsk Basin, Siberia, Russia. Palaeogeogr. Palaeoclim. Palaeoecol. 573, 110432.

Day, M.O., Rubidge, B.S., 2021. The late capitanian mass extinction of terrestrial verterbrates in the Karoo Basin of South Africa. Front. Earth Sci. 9, 631198.

Eldholm, O., Coffin, M.F., 2000. Large igneous provinces and plate tectonics. In: Richards, M., Gordon, R., Van der Hilst, R. (Eds.), The History and Dynamics of Global Plate Motions. AGU Geophys. Mon., pp. 309–326, 121.

Embry, A.F., Osadetz, K.G., 1988. Stratigraphy and tectonic significance of Cretaceous volcanism in Queen Elizabeth Islands, Canadian Arctic Archipelago. Can. J. Earth Sci. 25, 1209–1219.

Ernst, R.E., 2014. Large Igneous Provinces. Cambridge University Press, Cambridge, UK.

Firestone, R.B., 2020. The correlation between impact crater ages and chronostratigraphic boundary dates. Monthly Not. Royal Astron. Soc. 501, 3350–3363.

Gehrels, G.E., 2000. Introduction to detrital zircon studies of Paleozoic and Triassic strata in western Nevada and Northern California. Boulder, Colorado. Geol. Soc. Am. Spec. Paper 347, 1–7.

Glikson, A., 2005. Asteroid/comet impact clusters, flood basalts and mass extinctions: significance of isotopic age overlaps. Earth Planet. Sci. Lett. 236, 933–937.

Gomes, A.S., Vasconcelos, P.M., 2021. Geochronology of the Paran?-Etendeka large igneous province. Earth-Sci. Rev. 220, 103716.

Graziano, R., Raspini, A., Spalluto, L., 2013. High-resolution δ13C stratigraphy through the Selli Oceanic Anoxia Event (OAE1a) in the Apulia carbonate platform: the Borgo Celano section (western Gargano Promontory, Southern Italy). Italian J. Geosci. 132, 477–496.

Green, T., Renne, P.R., Keller, C.B., 2022. Continental flood basalts drive Phanerozoic extinctions. Proc. Natl. Acad. Sci. 119, e2120441119.

Hoernle, K., Hauff, F., Van den Bogaard, P., Werner, R., Mortimer, N., Geldmacher, J., Garbe-Schonberg, D., Davy, B., 2010. Age and geochemistry of volcanic rocks from the Hikurangi and Manihiki oceanic Plateaus. Geochim. Cosmochim. Acta 74, 7196–7219.

Husson, D., Galbrun, B., Laskar, J., Hinnov, L.A., Thibault, N., Gardin, S., Locklair, R.E., 2011. Astronomical calibration of the Maastrichian (Late Cretacaous). Earth Planet. Sci. Lett. 305, 328–340.

IPCC, 2018: Global Warming of 1.5°C. An IPCC Special Report on the impacts of global warming of 1.5°C above pre-industrial levels and related global greenhouse gas emission pathways, in the context of strengthening the global response to the threat of climate change, sustainable development, and efforts to eradicate poverty [Masson-Delmotte, V. et al., Eds.].

Ivanov, A.V., Corfu, F., Kamentsky, V.S., Marfin, A.E., Vladykin, N.V., 2021. ^{207}Pb-excess in carbonatitic baddeleyite as the result of Pa scavenging from the melt. Geochem. Perspect. Lett. 18, 11–15.

Ivanov, A.V., He, H., Yan, L., Ryabov, V.V., Shevko, A.Y., Palesskii, S.V., Nikolaeva, I.V., 2013. Siberian traps large igneous province: evidence for two flood basalt pulses around the Permo-Triassic boundary and in the Middle Triassic, and contemporaneous granitic magmatism. Earth-Sci. Rev. 122, 58–76.

Ivanov, A.V., Meffre, S., Thompson, J., Corfu, F., Kamenetsky, V.S., Kamenetsky, M.B., Demonterova, E.I., 2017. Timing and genesis of the Karoo-Ferrar large igneous province: new high precision U-Pb data for Tasmania confirm short duration of the major magmatic pulse. Chem. Geol. 455, 32–43.

Ivanov, B.A., Melosh, H.J., 2003. Impacts do not initiate volcanic eruptions: eruptions close to the crater. Geology 31, 869–872.

Jiang, Q., Jourdan, F., Olierook, H.K.H., Merle, R.E., 2023. An appraisal of the ages of Phanerozoic large igneous provinces. Earth-Sci. Rev. 237, 104314.

Johnston, S.T., Wynne, P.J., Francis, D., Hart, C.J.R., Enkin, R.J., Engebretson, D.C., 1996. Yellowstone in Yukon: the late cretaceous carmacks group. Geology 24, 997–1000.

Jourdan, F., Reimold, W.U., Deutsch, A., 2012. Dating terrestrial impact structures. Elements 8, 49–53.

Kasbohm, J., Schoene, B., 2018. Rapid eruption of the Columbia River flood basalt and correlation with the mid-Miocene climate optimum. Sci. Adv. 4, eaat8223.

Kenkmann, T., 2021. The terrestrial impact crater record: a statistical analysis of morphologies, structures, ages, lithologies, and more. Meteorit. Planet. Sci. 56, 1024–1070.

Kent, W., Saunders, A.D., Kempton, P.D., Ghose, N.C., 1997. Rajmahal basalts, eastern India: mantle sources and melt distribution at a volcanic rifted margin. In: Mahoney, J.J., Coffin, M.F. (Eds.), Large Igneous provinces: Continental, oceanic, and Planetary Flood Volcanism. AGU Geoph. Mon, pp. 145–182, 100.

Kerr, A.C., Tarney, J., Marriner, G.F., Nivia, A., Saunders, A.D., 1997. The Caribbean-Colombian cretaceous igneous province: the internal anatomy of an oceanic plateau. In: Mahoney, J.J., Coffin, M.F. (Eds.), Large Igneous provinces: Continental, oceanic, and Planetary Flood Volcanism. AGU Geoph. Mon, pp. 123–144, 100.

Koppers, A.A.P., Staudigel, H., Wijbrans, J.R., 2000. Dating crystalline groundmass separates of altered Cretaceous seamount basalts by the 40Ar/39Ar incremental heating technique. Chem. Geol. 166, 139–158.

Lapierre, H., Bosch, D., Dupuis, V., Polve, M., Maury, R.C., Hernandez, J., Monie, P., Yeghicheyan, D., Jaillard, E., Tardy, M., Mercier de Lepinay, B., Mamberti, M., Desmet, A., Keller, F., Senebier, F., 2000. Multiple plume events in the genesis of the peri-Caribbean Cretaceous oceanic plateau province. J. Geophys. Res. 105, 8403–8421.

Larsen, L.M., Rex, D.C., Watt, W.S., Guise, P.G., 1999. 40Ar-39Ar dating of alkali basaltic dykes along the southwest coast of Greenland: cretaceous and Tertiary igneous activity along the eastern margin of the Labrador Sea, in Collected research papers, palaeontology, geochronology, geochemistry. Geol. Greenland Surv. Bull. 184, 19–29.

Lehmann, R., 2013. 3σ-Rule for outlier detection from the viewpoint of geodetic adjustment. J. Surv. Eng. 139, 157–165.

Li, Y., He, H., Ivanov, A.V., Demonterova, E.I., Pan, Y., Deng, C., Zheng, D., Zhu, R., 2018. ^{40}Ar/^{39}Ar age of the onset of high-Ti phase of the Emeishan volcanism strengthens the link with the end-Guadalupian mass extinction. Int. Geol. Rev. 60, 1906–1917.

Methner, K., Campani, M., Fiebig, J., Loffler, N., Kempf, O., Mulch, A., 2020. Middle Miocene long-term continental temperature change in and out of pace with marine climate records. Sci. Rep. 10, 7989.

Mihalynuk, M.G., Erdmer, P., Ghent, E.D., Archibald, D.A., Friedman, R.M., Cordey, F., Johannson, G.G., Beanish, J., 1997. Age constraints for emplacement of the northern Cache Creek terrane and implications of blueschist metamorphism, in British Columbia Geological Survey Branch, Geological Fieldwork 1198-1.

Mittal, T., Sprain, C.J., Renne, P.R., Richards, M.A., 2022. Deccan volcanism at K-Pg time. In: Koeberl, C., Claeys, P., Montanari, A. (Eds.), From the Guajira Desert to the Apennines, and from Mediterranean Microplates to the Mexican Killer Asteroid: Honoring the Career of Walter Alvarez. Geol. Soc. America Spec. Paper 557, pp. 471–496.

Mortensen, J.K., Hulbert, L., 1992. A U-Pb zircon age for a Maple Creek gabbro sill, Tatamagouche Creek area, southwest Yukon Territory, in Radiogenic age and Isotopic studies, Report 5. Geol. Surv. Canada 91-2, 175–179.

Neal, C.R., Mahoney, J.J., Kroenke, L.W., Duncan, R.A., Petterson, M.G., 1997. The Ontong Java plateau. In: Mahoney, J.J., Coffin, M.F. (Eds.), Large Igneous provinces: Continental, Oceanic and Planetary Flood Volcanism. AGU Geoph. Mon, pp. 183–216, 100.

Ogren, P.J., Meetze, A., Duer, W.C., 2009. The limit of detection in generalized least-squares calibrations: an example using alprazolam liquid chromatography-tandem mass spectrometry data. J. Anal. Toxicol. 33, 129–142.

Oresic, L.S., Grdinic, V., 1990. Kaiser's 3-sigma criterion: a review of the limit of detection. Acta Pharm. Jugosl. 40, 21–61.

Pallister, J.S., Budahn, J.R., Murchey, B.L., 1989. Pillow basalts of the Angayucham terrane: oceanic plateau and island crust accreted to the Brooks Range. J. Geophys. Res. 94, 15901–15923.

Parkinson, I.J., Schaefer, B.E., Arculus, R.J., 2002. A lower mantle origin for the world's biggest LIP? A high precision Os isotope isochron from Ontong Java Plateau basalts drilled on ODP Leg 192. Geochim. Cosmochim. Acta 66, A580.

Pavlov, V.E., Fluteau, F., Latyshev, A.V., Fetisova, A.M., Elkins-Tanton, L.T., Black, B.A., Burgess, S.D., Veselovskiy, R.V., 2019. Geomagnetic secular variations at the Permian-Triassic boundary and pulsed magmatism During eruption of the Siberian Traps. Geochem. Geophys. Geosyst. 20, 773–791.

Phipps Morgan, J., Reston, T.J., Ranero, C.R., 2004. Contemperaneous mass extinctions, continental flood basalts, and 'impact signals': are mantle plume-induced lithospheric gas explosions the Causal link? Earth Planet. Sci. Lett. 217, 263–284.

Pimiento, C., Griffin, J.N., Clements, C.F., Silvestro, D., Varela, S., Uhen, M.D., Jaramillo, C., 2017. The Pliocene marine megafauna extinction and its impact on functional diversity. Nat. Ecol. Evol. 1. https://doi.org/10.1038/s41559-017-0223-6.

Powerman, V.I., Buyantuev, M.D., Ivanov, A.V., 2021. A review of detrital zircon data treatment, and launch of a new tool 'Dezirteer' along with the suggested universal workflow. Chem. Geol. 583, 120437.

Renne, P.R., Sprain, C.J., Richards, M.A., Self, S., Vanderkluysen, L., Pande, K., 2015. State shift in Deccan volcanism at the Cretaceous-Paleogene boundary, possibly induced by impact. Science 350, 76–78.

Retallack, G.J., Conde, G.D., 2020. Deep time perspective on rising atmospheric CO_2. Glob. Planet. Change 189, 103177.

Rey, S.S., Planke, S., Symonds, P.A., Faleide, J.I., 2008. Seismic volcano stratigraphy of the Gascoyne margin, Western Australia. J. Volc. Geoth. Res. 172, 112–131.

Richards, M.A., Alvarez, W., Self, S., Karlstrom, L., Renne, P.R., Manga, M., Sprain, C.J., Smit, J., Vanderkluysen, L., Gibson, S.A., 2015. Triggering of the largest Deccan eruptions by the Chicxulub impact. GSA Bull. 127, 1507–1520.

Sahy, D., Hiess, J., Fischer, A.U., Condon, D.J., Terry Jr., D.O., Abels, H.A., Husing, S.K., Kuiper, K.F., 2020. Accuracy and precision of the late Eocene-early Oligocene geomagnetic polarity time scale. GSA Bull. 132, 373–388.
Satkoski, A.M., Wilkinson, B.H., Hieptas, J., Samson, S.D., 2013. Likeness among detrital zircon populations – An approach to the comparison of age frequency data in time and space. Geol. Soc. Am. Bull. 125, 1783–1799.
Saylor, J.E., Sundell, K.E., 2016. Quantifying comparison of large detrital geochronology data sets. Geosphere 12, 203–220.
Schmieder, M., Kring, D.A., 2020. Earth's impact events through geologic time: a list of recommended ages for terrestrial impact structures and deposits. Astrobiology 2020 (1).
Schoene, B., Eddy, M.P., Samperton, K.M., Keller, C.B., Keller, G., Adatte, T., Khadri, S.F. R., 2019. U-Pb constraints on pulsed eruption of the Deccan Traps across the end-Cretaceous mass extinction. Science 363, 862–866.
Schoepfer, S.D., Algeo, T.J., Van de Schootbrugge, B., Whiteside, J.H., 2022. The Triassic-Jurassic transition – A review of environmental change at the dawn of modern life. Earth-Sci. Rev. 232, 104099.
Scott, R.W., 2014. A Cretaceous chronostratigraphic database: construction and applications. Carnets Geol. 14 (2).
Sell, B., Ovtcharova, M., Guex, J., Bartolini, A., Jourdan, F., Spangenberg, J.E., Vicente, J.-C., Schaltegger, U., 2014. Evaluating the temporal link between the Karoo LIP and climatic-biologic events of the Toarcian stage with high-precision U-Pb geochronology. Earth Planet. Sci. Lett. 408, 48–56.
Sharman, G.R., Sharman, J.P., Sylvester, Z., 2018. detritalPy: a Python-based toolset for visualizing and analysing detrital geo-thermochronologic data. Deposit. Rec. 4, 202–215.
Sheth, H., Pande, K., Vijayan, A., Sharma, K.K., Cucciniello, C., 2017. Recurrent early cretaceous, indo-madagascar (89-86 Ma) and Deccan (66 Ma) alkaline magmatism in the Sarnu-Dandali complex, Rajasthan: $^{40}Ar/^{39}Ar$ age evidence and geodynamic significance. Lithos 284-285, 512–524.
Smith, A.B., Gale, A.S., Monks, N.E.A., 2001. Sea-level change and rock-record bias in the cretaceous: a problem for extinction and biodiversity studies. Paleobiology 27, 241–253.
Sobolev, S.V., Sobolev, A.V., Kuzmin, D.V., Krivolutskaya, N.A., Petrunin, A.G., Arndt, N. T., Radko, V.A., Vasiliev, Y.R., 2011. Linking mantle plumes, large igneous provinces and environmental catastrophes. Nature 477, 312–316.
Storey, B.C., Leat, P.T., Weaver, S.D., Pankhurst, R.J., Bradshaw, J.D., Kelley, S., 1999. Mantle plumes and Antarctica–New Zealand rifting: evidence from mid-Cretaceous mafic dykes. J. Geol. Soc. Lond. 156, 659–671.
Storey, M., Mahoney, J.J., Saunders, A.D., Duncan, R.A., Kelley, S.P., Coffin, M.F., 1995. Timing of hot spot-related volcanism and the breakup of Madagascar and India. Science 267, 852–855.
Sundell, K.E., Saylor, J.E., 2017. Unmixing detrital geochronology age distributions. Geochem. Geophys. Geosyst. 18, 2872–2886.
Sundell, K.E., Saylor, J.E., 2021. Two-dimensional quantitative comparison of density distributions in detrital geochronology and geochemistry. Geochem. Geophys. Geosyst. 22 e2020GC009559.
Takashima, R., Nishi, H., Yoshida, T., 2006. Late Jurassic-early cretaceous intra-arc sedimentation and volcanism linked to plate motion change in Northern Japan. Geol. Mag. 143, 753–770.
Tarduno, J.A., Brinkman, D.B., Renne, P.R., Cottrell, R.D., Scher, H., Castillo, P., 1998. Late cretaceous arctic volcanism: tectonic and climatic consequences (abstract). In: AGU Spring Meeting, p. S63.
Tye, A.R., Wolf, A.S., Niemi, N.A., 2019. Bayesian population correlation: a probabilistic approach to inferring and comparing population distributions for detrital zircon ages. Chem. Geol. 518, 67–78.
Van der Boon, A., Kuiper, K.F., Van der Ploeg, R., Cramwinckel, M.J., Honarmand, M., Sluijs, A., Krijgsman, W., 2021. Exploring a link between the Middle Eocene Climatic Optimum and Neotethys continental arc flare-up. Clim. Past 17, 229–239.
Vermeesch, P., 2013. Multi-sample comparison of detrital age distributions. Chem. Geol. 341, 140–146.
Vermeesch, P., 2018a. Dissimilarity measures in detrital geochronology. Earth-Sci. Rev. 178, 310–321.
Vermeesch, P., 2018b. IsoplotR: a free and open toolbox for geochronology. Geosci. Front. 9, 1479–1493.
Vogt, P.R., 1972. Evidence for global synchronism in mantle plume convection, and possible significance for geology. Nature 240, 338–342.
Walkden, G., Parker, J., 2008. The biotic effects of large bolide impacts: size versus time and place. Int. J. Astrobiol. 7, 209–215.
Wasserstein, R.L., Schirm, A.L., Lazar, N.A., 2019. Moving to a world beyond "$\rho<0.05$". Am. Statist. 73, 1–19.
Westerhold, T., Rohl, U., McCarren, H.K., Zachos, J.C., 2009. Latest on the absolute age of the Paleocene-Eocene thermal maximum (PETM): new insights from exact stratigraphic position of key ash layers +19 and -17. Earth Planet. Sci. Lett. 287, 412–419.
Wu, Q., Zhang, H., Ramezani, J., Zhang, F.-F., Erwin, D.H., Feng, Z., Shao, L.-Y., Cai, Y.-F., Zhang, S.-H., Xu, Y.-G., Shen, S.-Z., 2024. The terrestrial end-Permian mass extinction in the paleotropics post-dates the marine extinction. Sci. Adv. 10 sciadv.adi7284.
Zhong, Y.T., Luo, Z.-Y., Mundil, R., Wei, X., Liu, H.-Q., He, B., Huang, X.-L., Tian, W., Xu, Y.-G., 2021. Constraining the duration of the Tarim flood basalts (northwestern China): CA-TIMS zircon U-Pb dating of tuffs. GSA Bull. 134, 325–334.